Spatio-temporal distribution of fault slip and high-frequency radiation of the 2010 El Mayor-Cucapah, Mexico earthquake

Takahiko Uchide,[1,2,*] Huajian Yao,[3,2] and Peter M. Shearer[2]

[1] Earthquake slip history and moment release are best resolved using long period seismic waves, but details in the rupture process, such as sharp changes in rupture velocity or direction, can be imaged more clearly using higher frequency waves. Here, we investigate the slip and the high-frequency radiation histories of the 2010 El Mayor-Cucapah, Baja California, Mexico earthquake (M_w 7.2). The slip distribution inferred from inversion of strong motion data between 0.02 and 0.25 Hz indicates northwest propagating rupture, followed by bilateral rupture for 40 s. The sources of high-frequency radiation between 0.3 and 2 Hz inferred from back-projection analysis using teleseismic data are adjacent to, but not within, the high-slip patches from the finite slip model in time and space. This implies relatively smooth rupture during the times and regions of maximum moment release. As theoretical models have predicted, high-frequency radiation seems mostly associated with changes in rupture velocity or slip magnitude. Strong high-frequency radiation is also found where the rupture propagated to a branch fault 50-km northwest of the hypocenter. Complementary constraints on both fault slip and high-frequency radiation provide increased understanding of earthquake rupture mechanics and may help improve strong motion evaluation at high frequencies.

Citation: Uchide, T., H. Yao, and P. M. Shearer (2013), Spatio-temporal distribution of fault slip and high-frequency radiation of the 2010 El Mayor-Cucapah, Mexico earthquake, *J. Geophys. Res. Solid Earth*, *118*, doi:10.1002/jgrb.50144.

1. Introduction

[2] Seismic data in different frequency bands often yields different images of the seismic rupture process. The location of high-frequency radiation sources relative to the fault slip inferred from the low-frequency seismograms and geodetic data has been studied using analyses of the envelope functions [*Zeng et al.*, 1993; *Kakehi and Irikura*, 1996; *Kakehi et al.*, 1996; *Kakehi and Irikura*, 1997; *Nakahara et al.*, 1998, 1999, 2002], wavelets [*Suzuki and Iwata*, 2009], and waveform back projection [*Allmann and Shearer*, 2007]. These studies have detected high-frequency radiation around the edge of large slip patches and the step over of faults, while high-frequency radiation has also been found around rupture initiation points, surface ruptures, and sometimes within large slip areas [*Nakahara*, 2008; H. Nakahara, personal communication, 2012]. Note that the term "high-frequency" radiation is not strictly defined, and different studies often define the high-frequency band differently, particularly when they involve different magnitude earthquakes. For studies of M 6–8 earthquakes, the high-frequency band is typically around 1 Hz or higher, a band in which earthquake engineering is also interested.

[3] The 2011 Tohoku earthquake exhibited frequency-dependent rupture behavior: the fault slip was greatest in the shallower part near the Japan Trench, whereas the radiation at higher frequencies was mainly from the deeper part of the fault [*Koper et al.*, 2011; *Meng et al.*, 2011b; *Simons et al.*, 2011; *Wang and Mori*, 2011; *Yao et al.*, 2011, 2012; *Kiser and Ishii*, 2012; *Roten et al.*, 2012]. *Lay et al.* [2012] pointed out that variations of rupture properties with depth are also found in other recent megathrust earthquakes.

[4] The frequency dependence of seismic radiation constrains the dynamics of the rupture process. An experiment to observe fracturing of a glass plate found high-frequency radiation in a dilatational wave associated with the stoppage [*Savage and Hasegawa*, 1964]. Seismograms of natural earthquakes also contain such high-frequency pulses, often referred as stopping phases [*Savage*, 1965]. Numerical studies imply that high-frequency radiation comes from the end of the crack [*Madariaga*, 1977] and from rapid changes in the rupture or slip velocity [*Yamashita*, 1983; *Spudich and Frazer*, 1984; *Sato*, 1994]. Spatial variations in the prestress and strength of the fault cause spatial variations in the rupture velocity [e.g., *Day*, 1982], which produce increased high-frequency radiation. Complexities in fault

[1]Disaster Prevention Research Institute, Kyoto University, Uji, Kyoto, Japan.
[2]Institute of Geophysics and Planetary Physics, Scripps Institution of Oceanography, University of California, San Diego, California, USA.
[3]Laboratory of Seismology and Physics of Earth's Interior, School of Earth and Space Sciences, University of Science and Technology of China, Hefei, Anhui, China.
[*]Now at Geological Survey of Japan, National Institute of Advanced Science and Technology, Tsukuba, Ibarak, Japan.

Corresponding author: T. Uchide, Geological Survey of Japan, AIST Tsukuba Central 7, 1-1-1 Higashi, Tsukuba, Ibaraki 305-8567, Japan. (uchide@eqh.dpri.kyoto-u.ac.jp)
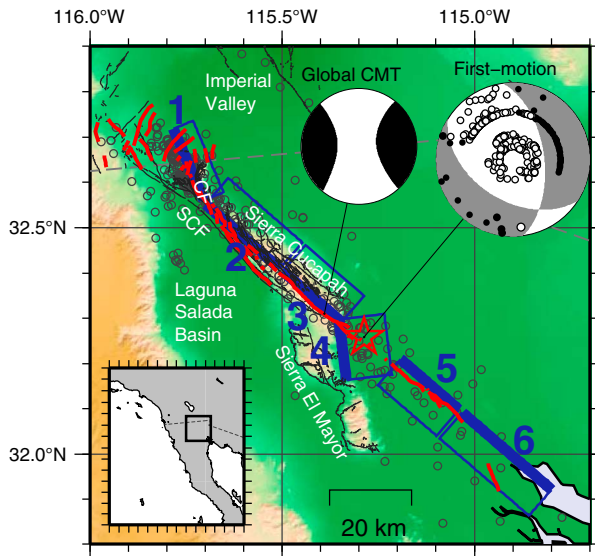
Figure 1. Map of the source region of the 2010 El Mayor-Cucapah earthquake. The gray circles show the aftershock seismicity within 6 h of the main shock from a relocated catalog [*Lin et al.*, 2007; *Hauksson et al.*, 2012]. The beach balls show the CMT solution by the Global CMT project and the first-motion focal mechanism obtained by this study. The closed and open circles on the beach ball for the first motion solution indicate positive and negative polarities, respectively, at individual stations. The black lines are the surface trace of faults from *Fletcher and Spelz* [2009] and U.S. Geological Survey and California Geological Survey (Quaternary fault and fold database for the United States, 2012, http://earthquakes.usgs.gov/regional/qfaults/). The red lines indicate the surface rupture of the 2010 El Mayor-Cucapah earthquake from *Rymer et al.* [2010] and *Fletcher et al.* [2010]). The numbered blue boxes show the projection of the fault segments used in this study for the seismic slip inversion analysis (Table 2) onto the ground surface, and the thick lines show the shallowest portion of the fault segments. Note the geometry of segments #2 and #3, and #5 and #6 are same, respectively, but that different model expansion speeds are given to capture the rupture process efficiently (see Table 2). The dashed gray line indicates the international border between Mexico and the United States. The inset map shows Baja California and Southern California, and the box in the map indicates the area of the main map. CF and SCF denote Centinela fault and Sierra Cucapah fault, respectively.

geometry, such as a fault kink or a coalescence of multiple cracks, also cause high-frequency radiation [*Adda-Bedia and Madariaga*, 2008; *Kame and Uchida*, 2008; *Dunham et al.*, 2011]. To understand the dynamic rupture process, it is important to understand the relationship between fault slip and high-frequency radiation, not only in space but also in time.

[5] This paper studies the 2010 El Mayor-Cucapah, Baja California, Mexico earthquake (*M* 7.2) that occurred at 22:40 on 4 April 2010 (UTC). Figure 1 shows the source region of this earthquake. The fault system has been investigated in detail [e.g., *Fletcher and Spelz*, 2009]. On the western side of the Sierra Cucapah and Sierra El Mayor, the fault is well developed. Seismic data are available

from both strong-motion stations in Southern California, the United States, and Baja California, Mexico, and from teleseismic stations of the Global Seismic Network (GSN). The centroid moment tensor (CMT) solutions from the Global CMT Project indicate mostly right-lateral strike-slip but with substantial Compensated Linear Vector Dipole components. A focal mechanism solution from high-rate GPS data also indicates a right-lateral strike-slip faulting [*Zheng et al.*, 2012]. According to slip inversion results [*Wei et al.*, 2011], aftershock distributions [*Castro et al.*, 2011; *Hauksson et al.*, 2011; *Hauksson et al.*, 2012], field observations of surface rupture [*Fletcher et al.*, 2010], and remote sensing using SAR [*Fialko et al.*, 2010; *Wei et al.*, 2011; *Okamoto*, 2012] and light detection and ranging (LiDAR) [*Oskin et al.*, 2012], the earthquake started east of Sierra El Mayor, Mexico, ruptured along the Sierra Cucapah fault, jumped to the Centinela fault with a different strike angle from that of the Sierra Cucapah fault, and eventually reached the U.S.-Mexico border.

[6] This paper studies when and where the high-frequency seismic energy is radiated with respect to main slip patches, as constrained by both a finite slip inversion of long-period data and back-projection analysis of high-frequency waves. Based on these results, we discuss the implications of the high-frequency radiation pattern on earthquake physics.

2. Data

[7] Local strong-motion seismograms are recorded by the Southern California Seismic Network (SCSN) in the United States and by El Centro de Investigación Científica y de Educación Superior de Ensenada (CICESE) in Mexico. It should be noted that the two horizontal components of the original data at stations TRH, RSL, and CIC of CICESE strong-motion network are swapped, and the polarity of the vertical components of VTR, HDI, and GEO is flipped [*L. Orozco*, personal communication, 2010]. Figure 2 shows S waves recorded on the transverse components at selected stations (Table 1). The stations northwest of the epicenter recorded single sharp pulses (Figure 2a), while those in other directions recorded more dispersed waves. This implies strong directivity toward the northwest. However, such sharp pulses are observed 10–15 s after the initial S arrivals, suggesting a delay in the main moment release, a slow initial rupture velocity, or initial southeastward rupture propagation and then rerupture to the northwest (more about this later).

[8] The teleseismic data give a rough estimate of the source duration. A borehole seismic network in Japan, Hi-net [*Okada et al.*, 2004], recorded this earthquake very well. To make the signals clear, we align the P arrivals and stack the vertical components of the velocity seismograms from 781 stations, following corrections for instrument response. Figure 3a shows the stack of the Hi-net seismograms. The squared velocity envelope (Figure 3b) approximates the seismic energy radiated at the source. A strong peak is found around 25 s and substantial amplitudes are observed for 40 s. Since northwestward directivity is implied by the local strong-motion data and Hi-net stations are in that direction, this 40-s duration probably gives a minimum value.

[9] The polarity of the first P arrival of local and global data constrains the first motion focal mechanism, which reflects the mechanism of the first part of the rupture. We
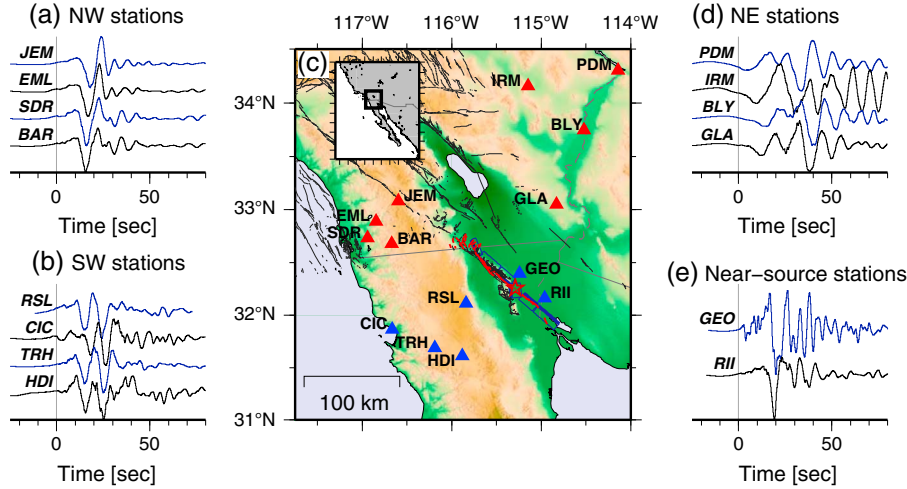
Figure 2. (a,b,d,e) Transverse components of displacement seismograms at selected stations. The displacement is obtained by integrating the acceleration records twice and high-pass filtering at 0.025 Hz to avoid low-frequency noise. (c) Map of the region around the fault, which spans the U.S.-Mexico border. The red and blue triangles indicate selected stations of the SCSN and CICESE strong-motion networks, respectively. The red star shows the epicenter of this earthquake. The black lines show the surface trace of faults from *Fletcher and Spelz* [2009] and U.S. Geological Survey and California Geological Survey (Quaternary fault and fold database for the United States, 2012, http://earthquakes. usgs.gov/regional/qfaults/), and the red lines indicate the surface rupture of the 2010 El Mayor-Cucapah earthquake from *Rymer et al.* [2010] and *Fletcher et al.* [2010] The blue boxes indicate the source model used by this study for the seismic slip inversion analysis.

manually picked the polarities and then computed a focal mechanism using the HASH code [*Hardebeck and Shearer*, 2002], assuming a pure double-couple focal mechanism. The estimated first motion focal mechanism shown in Figure 1 is between normal faulting and strike-slip, while the long-period Global CMT Project solution is mainly strike-slip. This implies rupture complexity with a different geometry for the initial slip compared to that of the dominant moment release.

3. Seismic Slip Inversion Analysis

3.1. Method and Data

[10] We apply the multi-time window slip inversion method [*Hartzell and Heaton*, 1983] to reveal the rupture

process of this earthquake. We use a fault model with six segments (Figure 1 and Table 2). We take the *x* axis toward the northwest along each segment and assign the range of *x* for each segment as shown in Table 2. The *y* axis is taken along dip. The origin corresponds to the rupture initiation point, which is at the SCSN epicenter (32.259°N, 115.287°W) at a depth of 9 km. The geometry of the initial rupture, segment #4, is one of the nodal planes of the

Table 1. Stations for the Seismic Slip Inversion Analysis[a]

Name	Latitude (N)	Longitude (W)	Structure
SCSN			
PDM	34.303	114.142	C
BLY	33.750	114.524	D
GLA	33.051	114.827	D
IRM	34.157	115.145	B
BAR	32.680	116.672	G
SDR	32.736	116.942	F
EML	32.891	116.846	E
JEM	33.081	116.598	E
CICESE			
GEO	32.400	115.240	A
RII	32.166	114.961	A
HDI	31.615	115.882	C
TRH	31.690	116.190	C
CIC	31.868	116.664	C
RSL	32.116	115.841	C

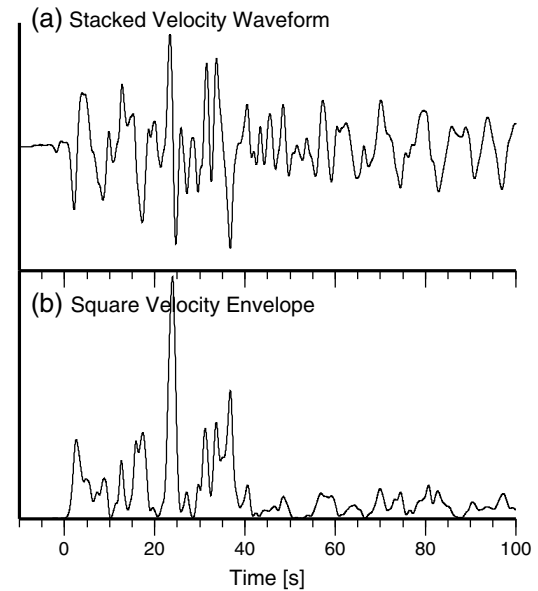[a] The structure used for each station is shown in Table 3.

Figure 3. (a) Velocity waveform obtained by stacking vertical components of Hi-net waveforms, and (b) its squared envelope, indicating the seismic energy rate history.

Table 2. Properties of Fault Segments[a]

	Strike	Dip	V_{exp} (km/s)	Length (km)	Width (km)	x (km)
#1	337	75	3.0	20	20	50–70
#2	311	65	3.0	25	20	25–50
#3	311	65	1.2	20	20	5–25
#4 (hypocenter)	353	56	3.0	15	20	−10 to 5
#5	311	115	3.0	20	20	−30 to −10
#6	311	115	1.0	30	20	−60 to −30

[a] V_{exp} denotes the model expansion speed.

first motion focal mechanism. The other parts follow the fault geometry inferred from the InSAR data [*Fialko et al.*, 2010]. Segment #1 corresponds to the Centinela fault with a different strike than the other segments. The total length and width of the fault model are 130 km and 20 km, respectively. The spatio-temporal slip-rate distribution is represented by a finite number of 1-D spline ("triangle") basis functions [see *Uchide and Ide*, 2007] with nodes spaced every 5 km in space and 2 s in time. Therefore, the basis functions span 10 km in space and 4 s in time and overlap for 5 km in space and 2 s in time with the adjacent basis functions. We set two model parameters for each node to represent rake angles of −45° and −135° allow slip directions between these limits. To reduce the number of free parameters, we specify the starting time of the first time window at each grid point. The first time window starts when a hypothetical rupture front expanding at a specified velocity (hereafter referred to as the "model expanding speed") arrives. The maximum duration of the slip model at each point is 30 s. Consequently, we have 25 nodes along strike, 4 along dip, and 14 in time. The total number of model parameters is 2800. In seismic slip inversion analysis, it is important to set the model expanding velocity to capture all slip patches in time and space. Note that the model expanding speed does not give the actual rupture velocity; instead, it represents the maximum permitted rupture velocity from the hypocenter. We determine the model expanding speed (Table 2) by trial and error to capture all rupture patches in time and space.

[11] We use 80-s displacement seismograms of 14 stations from SCSN and CICESE (Figure 2 and Table 1), integrate twice the original acceleration records, resample every 0.5 s, and bandpass-filter between 0.02 and 0.25 Hz. To compensate for poor coverage on the southeast of the source region, the data from station RII of the CICESE strong-motion network is weighed twice that of the other stations.

[12] Green's functions are calculated using a 1-D seismic velocity model using the reflection-transmission matrix [*Kennett and Kerry*, 1979] and the wavenumber integral [*Bouchon*, 1981] method. The effect of anelastic attenuation is modeled by using a complex seismic velocity [*Takeo*, 1985]. The 1-D seismic velocity structure for each station (Tables 1 and 3) is tuned to fit the seismograms of nearby M5 earthquakes. Note that these 1-D seismic velocity structures represent the velocity structure between the source region and the stations. Stations in the Salton Trough are not used, because it is difficult to reproduce the large surface waves and basin resonances with a 1-D model.

[13] We use a temporal smoothing constraint to stabilize the analysis [*Uchide and Ide*, 2007]. The strength of the smoothing constraint is set using Bayesian modeling in order to minimize the Akaike's Bayesian Information Criterion [*Akaike*, 1980; *Yabuki and Matsu'ura*, 1992]. In addition, the seismic moment is constrained to be equivalent to M_w 7.2, to match the Global CMT solution.

3.2. Result

[14] Figure 4 shows the estimated rupture process. The moment magnitude is 7.6×10^{19} Nm, equivalent to M_w 7.2, as constrained. Our inversion gives the moment rate distribution history, and we convert the moment rate to the slip rate,

Table 3. Seismic Velocity Structure for the Calculation of Green's Functions

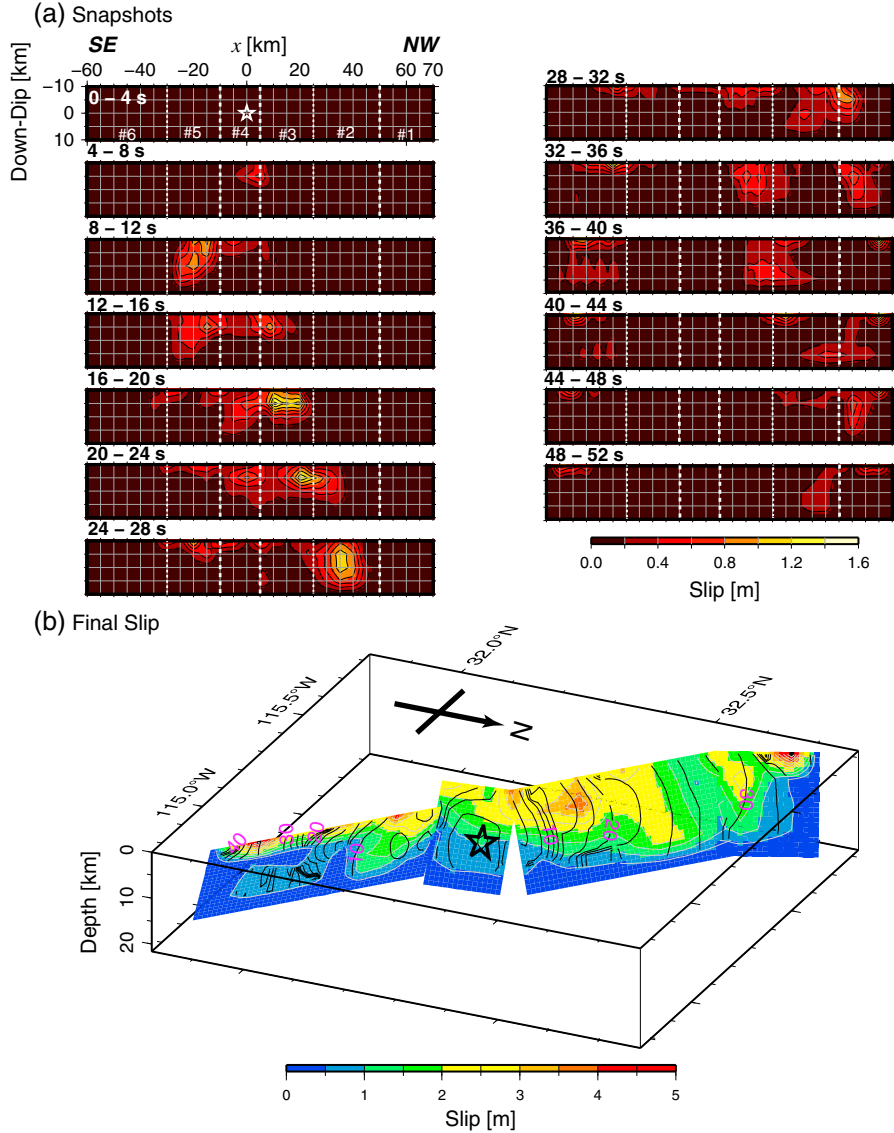| A (Depth [km]) V_p, V_s [km/s]	B (Depth [km]) V_p, V_s [km/s]	C (Depth [km]) V_p, V_s [km/s]	D (Depth [km]) V_p, V_s [km/s]	E (Depth [km]) V_p, V_s [km/s]	F (Depth [km]) V_p, V_s [km/s]	G (Depth [km]) V_p, V_s [km/s]
(0.0–2.0)	(0.0–1.5)	(0.0–1.0)	(0.0–1.0)		(0.0–0.5)	
2.0, 1.0	2.0, 1.0	2.0, 1.0	3.0, 1.5		3.0, 1.5	
(2.0–4.0)	(1.5–3.0)	(1.0–2.0)		(0.0–1.0)	(1.0–2.0)	
4.0, 2.0	4.0, 2.0	4.0, 2.0		4.0, 2.0	4.0, 2.0	
(4.0–5.5)	(3.0–4.0)	(2.0–3.0)	(1.0–1.5)	(1.0–2.0)		
5.0, 2.5	5.0, 2.5	5.0, 2.5	5.0, 2.5	5.0, 2.5		
(5.5–16.0)	(4.0–8.0)	(3.0–7.0)	(1.5–6.0)	(2.0–7.0)	(2.0–8.0)	(0.0–5.5)
6.0, 3.5	6.0, 3.5	6.0, 3.5	6.0, 3.5	6.0, 3.5	6.0, 3.5	5.5, 3.18
	(8.0–16.0)	(7.0–16.0)	(6.0–16.0)	(7.0–16.0)	(8.0–16.0)	(5.5–16.0)
	6.3, 3.64	6.3, 3.64	6.3, 3.64	6.3, 3.64	6.3, 3.64	6.3, 3.64
			(16.0–32.0)			
			6.7, 3.87			
			(32.0 -)			
			7.8, 4.50			

Figure 4. (a) Slip history and (b) final slip inferred from the seismic slip inversion analysis. Figure 4a shows the slip in consecutive 4-s time windows. In the first window, numbers such as #1 denote the names of the segments (Table 2). In Figure 4b, the black contours and pink numbers show the rupture time when cumulative slip reaches 5% of the final slip at specific point. The contour interval is 2 s.

assuming a uniform rigidity of 30 GPa, which is that in the lower crust in the Mojave Desert [*Pollitz*, 2003]. A reduction of rigidity may increase the slip amount. The maximum final slip is about 5 m (Figure 4b). This model explains the main features in the observed strong-motion waveforms quite well (Figure 5). The least-squares variance reduction is 72.8%.

[15] Most of the slip area is confined above 9 km, the depth of the hypocenter. Large slip patches are identified at and around the hypocenter, near $x = -40$, -20, 20, and 35 km. *Wei et al.* [2011] also identified large slip patches at similar locations. Note that the x axes of the slip model of *Wei et al.* [2011] and Figure 4 are in different configurations.

[16] Our model indicates that the rupture started near the hypocenter (segment #4) and propagated southeastward in the first 16 s. After that, the rupture propagated somewhat toward the northwest and at 20 s, the rupture began

propagating bilaterally. This time delay of the bilateral rupture reflects the delay of the sharp strong pulse observed in San Diego area to the northwest of the hypocenter area (Figure 2).

4. Back Projection Analysis

4.1. Method and Data

[17] The Green's functions for high-frequency seismic waves are not predicted well enough by current Earth models for these data to be useful in finite slip inversions. However, beam forming [e.g., *Krüger and Ohrnberger*, 2005] or back-projection methods [e.g., *Ishii et al.*, 2005] can be used to identify sources of high-frequency radiation during rupture. Here, we apply the back-projection method [*Ishii et al.*, 2005; *Yao et al.*, 2012] to teleseismic P waves
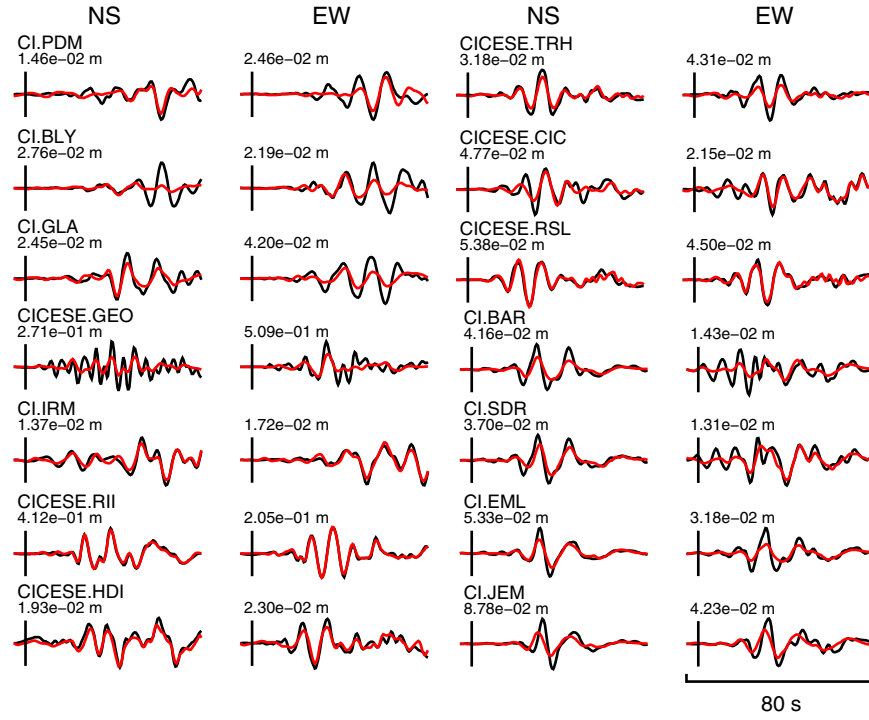
Figure 5. Waveform fit from the slip inversion. Black and red traces show the observed and synthetic waveforms, respectively. Numbers on the top left of the waveforms indicate the maximum amplitude of the observed waveforms. Vertical short lines indicate the S arrival.
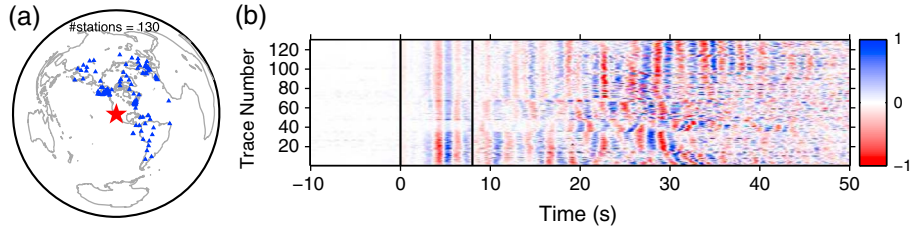

Figure 6. (a) Station distribution (blue triangles) for the iterative back projection. The red star gives the hypocenter location. (b) The aligned waveforms used for the back projection analysis. The two black lines show the first 8 s of the P waves for the initial waveform alignment using a cross-correlation method.
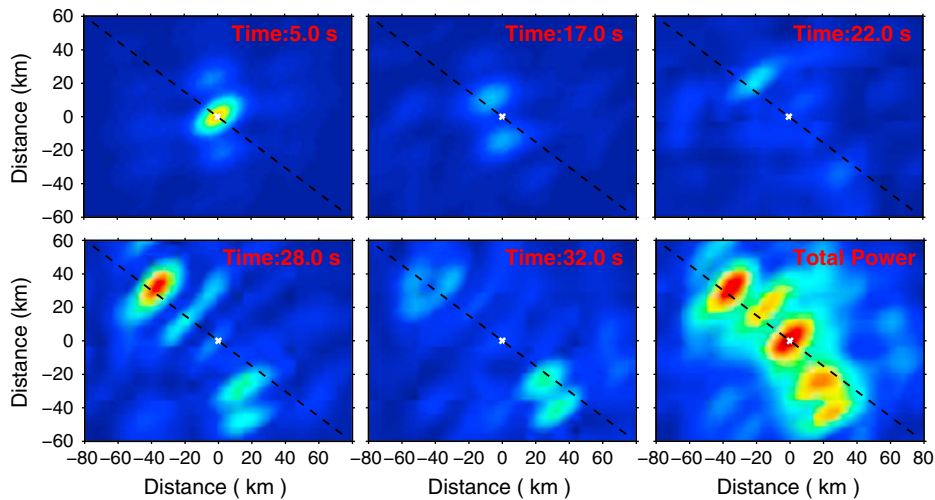

Figure 7. High-frequency (0.3–2 Hz) seismic radiation (map view) at five representative times as indicated and the total radiated power (lower right) from waveform back projection. The black dashed lines indicate the direction of N49W, the strike of the main part of the slip model (Table 2).

recorded by the global seismic network at epicentral distances between 30 and 95° to the hypocenter (Figure 6a).

[18] We apply a bandpass filter to the data between 0.3 and 2 Hz. Waveform cross-correlation for the initial few seconds of the P waves is used to align the waveforms to remove the effect of 3-D heterogeneity along the ray paths from the hypocenter to stations. We only use 130 traces with cross-correlation coefficients above 0.8 with respect to the first 8 s of the P wave stack for further back-projection analysis (Figure 6b). To suppress the effect of the uneven distribution of stations in the back-projection waveform stacking, we apply a station-weighting scheme [*Walker et al.*, 2005; *Walker and Shearer*, 2009], in which the waveform for a given station is weighted by the inverse of the number of other stations within 400 km.

[19] We back project the recorded waveforms to a regular 2-D lateral grid in the source region (2 km spacing). The time-dependent radiated power is estimated from the waveform stack power using a running-average windowing approach [*Yao et al.*, 2012].

4.2. Result

[20] Figure 7 summarizes the back projection results at a few representative times. The high-frequency seismic radiation clearly shows the bilateral rupture of this earthquake, with a total rupture extent about 100 km along strike. Strong high-frequency radiation between 0.3 and 2 Hz is observed near the hypocenter at the beginning of the rupture, 50 km northwest of the hypocenter at about 28 s, and also about 30 km southeast of the hypocenter at about 32 s. From the total back projection power, we can clearly identify five strong high-frequency sources, four of which are found along or very close to the fault. The high-frequency source at location (25, −40) km is about 20 km off the fault and occurred at a similar time as the subevent near (20, −20) km. This high-frequency source may represent an early aftershock that is not part of the primary rupture.

5. Discussion

[21] Figure 8 shows the spatiotemporal distribution of the high-frequency radiation inferred from the back projection analysis, relative to the moment release rate history inferred from the seismic slip inversion analysis. Since this fault is narrow, we focus on the variation along N49W, ignoring that along dip. Most of the high-frequency radiation is found near the beginning and end of the major moment release patches indicated by the red contours. The high-frequency radiation near the peaks in moment release rate is relatively minor. A strong pulse of high-frequency radiation around 50 km and 28 s is correlated to the step over from the Sierra Cucapah to the Centinela faults with different strike directions, or from segment #1 to #2, as expected from theoretical studies [*Adda-Bedia and Madariaga*, 2008].

[22] A repeated rupture between 5 and 40 km northwest of the hypocenter is inferred from the slip inversion result (dashed rectangles in Figure 8). Another rupture is seen 6 s after the main rupture passed, with some high-frequency radiation between the rupture pulses. How reliably is this repeated rupture patch resolved?
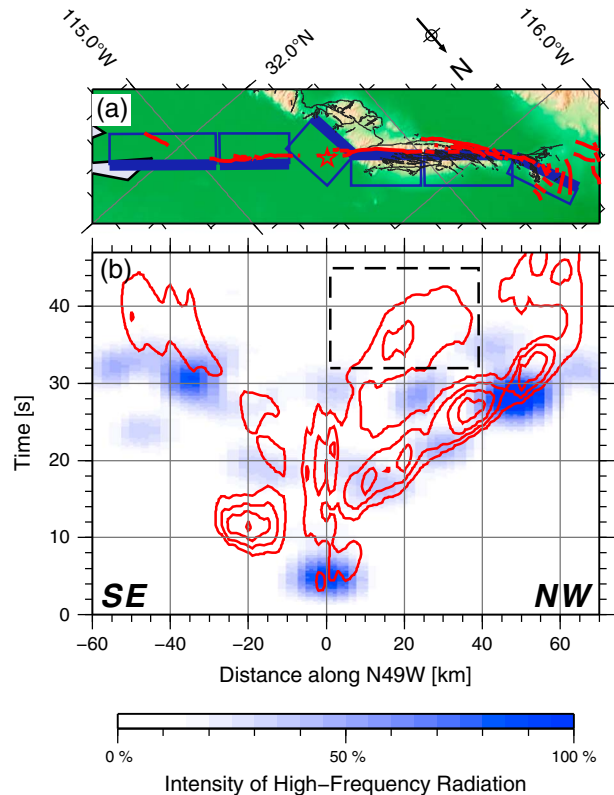

Figure 8. (a) Map of the source region rotated to align with N49°W. The blue boxes indicate the segments of the fault models for the slip inversion analysis. The red star shows the epicenter. The black lines are the surface trace of faults by *Fletcher and Spelz* [2009]. The red lines indicate the surface rupture of the 2010 El Mayor-Cucapah earthquake [*Fletcher et al.*, 2010]. (b) A comparison between the high-frequency radiation sources from the back projection analysis and the rupture process from the finite slip inversion. The blue image shows the spatio-temporal distribution of the high-frequency radiation intensity relative to the maximum value. The red contours show the moment rate per fault length, i.e., moment rate density integrated along dip. The contour interval is 5×10^{16} N/s (= (Nm/s)/m). The horizontal scale corresponds to the scale of the map (Figure 8a). The dashed rectangle indicates the repeated rupture in time and space that is discussed in Figure 9.

[23] The full model explains 72.8% of the root mean square (RMS) in the waveforms; the model without the repeated rupture patch explains 61.0% of the RMS. The fit is improved by more than 10% for PDM, BLY, and IRM of SCSN, and HDI, TRH, and RSL of CICESE strong-motion network (Figure 9). Thus, the repeated rupture patch contributes significantly to fitting the observed waveforms in our preferred model. However, we cannot rule out the possible existence of alternative models without the repeated rupture patch that could provide comparable fits to our full model. Thus, we consider this feature to be suggested by the data, but not yet definitively resolved. From the viewpoint of earthquake source physics, repeated ruptures are possible [e.g., *Gabriel et al.*, 2012], and a repeated rupture has been found during the 2011 Tohoku earthquake [e.g.,
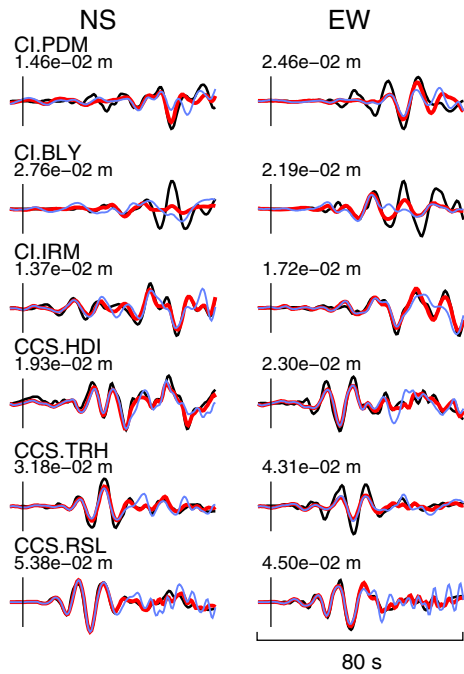
Figure 9. Waveforms at selected stations from the model without the repeated rupture inferred from the slip inversion. Black, red, and blue traces show the observed waveforms, the synthetic waveforms from the full model, and the model without the repeated rupture, respectively. Numbers on the top left of the waveforms indicate the maximum amplitude of the observed waveforms. Vertical short lines indicate the S arrival. Notice that the model with the repeated rupture (red curve) provides a better fit than when this feature is left out (blue curve).

Lee et al., 2011]. In the case of the 2010 El Mayor-Cucapah earthquake, repeated rupture was suggested from a back projection study using regional data from USArray and the Seismic Investigation of Edge Driven Convection Associated with the Rio Grande Rift Array in and around New Mexico [*Meng et al.*, 2011a].

[24] Prior studies have investigated the anti-correlation between the fault slip and the high-frequency radiation distributions in space. High-frequency radiation has been observed near the edge of high-slip areas in earthquakes between M6 and M8: the 1993 Loma Prieta (*M* 7.1) [*Zeng et al.*, 1993], the 1993 Kushiro-oki (M_w 7.6) [*Kakehi and Irikura*, 1996], the 1993 southwest off Hokkaido (M_w 7.5) [*Kakehi and Irikura*, 1997], the 1994 far-off Sanriku [*Nakahara et al.*, 1998], the 1995 Kobe (M_w 6.9) [*Kakehi et al.*, 1996; *Nakahara et al.*, 1999], the 1998 Iwate (M_j 6.1) [*Nakahara et al.*, 2002], the 2000 Tottori (M_w 6.6) [*Suzuki and Iwata*, 2009], and the 2004 Parkfield (M_w 6.0) [*Allmann and Shearer*, 2007] earthquakes. Our result reveals the same features in the 2010 El Mayor-Cucapah earthquake (M_w 7.2), not only in space but also in time. It is expected from theoretical studies that rapid changes in rupture velocity or slip velocity will cause stronger high-frequency radiation [*Yamashita*, 1983; *Spudich and Frazer*, 1984; *Sato*, 1994]. Our comparison between the slip model and the high-frequency radiation distribution history in space and time reveals that the high-frequency seismic

waves are radiated both from the beginning and the end of ruptures.

[25] The anti-correlation between the moment release and the high-frequency radiation implies that the rupture velocity during the periods of maximum moment release is stable [*Spudich and Frazer*, 1984]. Thus, the effects of fault details (such as fault roughness [*Adda-Bedia and Madariaga*, 2008; *Kame and Uchida*, 2008; *Dunham et al.*, 2011] and heterogeneities of the initial stress on the fault [*Day*, 1982]) on rupture velocity are apparently weak or effectively averaged out during the main moment release period. This may help in understanding large-slip events, even when we do not image the small-scale details of the rupture process.

6. Conclusions

[26] We examine the fault slip and the high-frequency radiation distribution history of the 2010 El Mayor-Cucapah earthquake by comparing a slip inversion from strong-motion data and high-frequency back projection of teleseismic data, not only in space but also in time. Peaks in high-frequency radiation are seen adjacent to, rather than within, the regions of highest slip. This fact implies that the rupture velocity during the major rupture episodes is stable. Substantial high-frequency radiation is also observed near a change in fault direction. These results should help constrain dynamic rupture simulations for this earthquake, and complementary studies of this type eventually may help to improve strong ground motion predictions at the high frequencies that often lead to the greatest damage to buildings.

References

Adda-Bedia, M., and R. Madariaga (2008), Seismic radiation from a kink on an antiplane fault, *Bull. Seismol. Soc. Am.*, *98*(5), 2291–2302, doi:10.1785/0120080003.

Akaike, H. (1980), Likelihood and the Bayes procedure, in *Baysian Statistics*, edited by J. M. Bernardo, M. H. DeGroot, D. V. Lindley and A. F. M. Smith, pp. 143–166, Univ. Press, Valencia, Spain.

Allmann, B. P., and P. M. Shearer (2007), A high-frequency secondary event during the 2004 Parkfield earthquake, *Science*, *318*(5854), 1279–1283, doi:10.1126/science.1146537.

Bouchon, M. (1981), A simple method to calculate Green's functions for elastic layered media, *Bull. Seismol. Soc. Am.*, *71*(4), 959–971.

Castro, R. R., J. G. Acosta, V. M. Wong, A. Pérez-Vertti, A. Mendoza, and L. Inzunza (2011), Location of aftershocks of the 4 April 2010 M_w 7.2 El Mayor–Cucapah earthquake of Baja California, Mexico, *Bull. Seismol. Soc. Am.*, *101*(6), 3072–3080, doi:10.1785/0120110112.

Day, S. M. (1982), Three-dimensional simulation of spontaneous rupture: The effect of nonuniform prestress, *Bull. Seismol. Soc. Am.*, *72*(6A), 1881–1902.

Dunham, E. M., D. Belanger, L. Cong, and J. E. Kozdon (2011), Earthquake ruptures with strongly rate-weakening friction and off-fault plasticity, part 2: Nonplanar faults, *Bull. Seismol. Soc. Am.*, *101*(5), 2308–2322, doi:10.1785/0120100076.

Fialko, Y., A. Gonzalez, J. Gonzalez, S. Barbot, S. Leprince, D. Sandwell, and D. Agnew (2010), Static rupture model of the 2010 M7.2 El Mayor-Cucapah earthquake from ALOS, ENVISAT, SPOT and GPS data, paper presented at Southern California Earthquake Center 2010 Annual Meeting, Palm Springs, CA.

Fletcher, J. M., and R. M. Spelz (2009), Patterns of quaternary deformation and rupture propagation associated with an active low-angle normal fault, Laguna Salada, Mexico: Evidence of a rolling hinge?, *Geosphere*, 5(4), 385–407, doi:10.1130/ges00206.1.

Fletcher, J. M.et al. (2010). Kinematic and dynamic analysis of the Mayor-Cucapah Earthquake: A case for 3-D strain accommodation in a single earthquake cycle, Abstract T51E-07 presented at 2010 Fall Meeting AGU, San Francisco, CA.

Gabriel, A. A., J. P. Ampuero, L. A. Dalguer, and P. M. Mai (2012), The transition of dynamic rupture styles in elastic media under velocity-weakening friction, *J. Geophys. Res.*, 117(B9), B09311, doi:10.1029/2012JB009468.

Hardebeck, J. L., and P. M. Shearer (2002), A new method for determining first-motion focal mechanisms, *Bull. Seismol. Soc. Am.*, 92(6), 2264–2276.

Hartzell, S. H., and T. H. Heaton (1983), Inversion of strong ground motion and teleseismic waveform data for the fault rupture history of the 1979 Imperial Valley, California, earthquake, *Bull. Seismol. Soc. Am.*, 73(6A), 1553–1583.

Hauksson, E., J. Stock, K. Hutton, W. Yang, J. Vidal-Villegas, and H. Kanamori (2011), The 2010 M_w 7.2 El Mayor-Cucapah earthquake sequence, Baja California, Mexico and Southernmost California, USA: Active seismotectonics along the Mexican Pacific Margin, *Pure appl. Geophys.*, 168(8), 1255–1277, doi:10.1007/s00024-010-0209-7.

Hauksson, E., W. Yang, and P. M. Shearer (2012), Waveform relocated earthquake catalog for Southern California (1981 to June 2011), *Bull. Seismol. Soc. Am.*, 102(5), 2239–2244, doi:10.1785/0120120010.

Ishii, M., P. M. Shearer, H. Houston, and J. E. Vidale (2005), Extent, duration and speed of the 2004 Sumatra-Andaman earthquake imaged by the Hi-Net array, *Nature*, 435(7044), 933–936.

Kakehi, Y., and K. Irikura (1996), Estimation of high-frequency wave radiation areas on the fault plane by the envelope inversion of acceleration seismograms, *Geophys. J. Int.*, 125(3), 892–900.

Kakehi, Y., and K. Irikura (1997), High-frequency radiation process during earthquake faulting – Envelope inversion of acceleration seismograms from the 1993 Hokkaido-Nansei-Oki, Japan, Earthquake, *Bull. Seismol. Soc. Am.*, 87(4), 904–917.

Kakehi, Y., K. Irikura, and M. Hoshiba (1996), Estimation of high-frequency wave radiation areas on the fault plane of the 1995 Hyogo-ken Nanbu earthquake by the envelope inversion of acceleration seismograms, *J. Phys. Earth*, 44(5), 505–517.

Kame, N., and K. Uchida (2008), Seismic radiation from dynamic coalescence, and the reconstruction of dynamic source parameters on a planar fault, *Geophys. J. Int.*, 174(2), 696–706, doi:10.1111/j.1365-246X.2008.03849.X.

Kennett, B. L. N., and N. J. Kerry (1979), Seismic waves in a stratified half space, *Geophys. J. R. astr. Soc.*, 57(3), 557–583.

Kiser, E., and M. Ishii (2012), The March 11, 2011 Tohoku-oki earthquake and cascading failure of the plate interface, *Geophys. Res. Lett.*, 39, L00G25, doi:10.1029/2012GL051170.

Koper, K. D., A. R. Hutko, T. Lay, C. J. Ammon, and H. Kanamori (2011), Frequency-dependent rupture process of the 11 March 2011 M_W 9.0 Tohoku earthquake: Comparison of short-period P wave backprojection images and broadband seismic rupture models, *Earth Planets Space*, 63, 599–602.

Krüger, F., and M. Ohrnberger (2005), Spatio-temporal source characteristics of the 26 December 2004 Sumatra earthquake as imaged by teleseismic broadband arrays, *Geophys. Res. Lett.*, 32(24), L24312, doi:10.1029/2005GL023939.

Lay, T., H. Kanamori, C. J. Ammon, K. D. Koper, A. R. Hutko, L. Ye, H. Yue, and T. M. Rushing (2012), Depth-varying rupture properties of subduction zone megathrust faults, *J. Geophys. Res.*, 117(B4), B04311, doi:10.1029/2011JB009133.

Lee, S.-J., B.-S. Huang, M. Ando, H.-C. Chiu, and J.-H. Wang (2011), Evidence of large scale repeating slip during the 2011 Tohoku-Oki earthquake, *Geophys. Res. Lett.*, 38(19), L19306, doi:10.1029/2011GL049580.

Lin, G. Q., P. M. Shearer, and E. Hauksson (2007), Applying a three-dimensional velocity model, waveform cross correlation, and cluster analysis to locate southern California seismicity from 1981 to 2005, *J. Geophys. Res.*, 112(B12), B12309, doi:10.1029/2007JB004986.

Madariaga, R. (1977), High-frequency radiation from crack (stress drop) models of earthquake faulting, *Geophys. J. R. astr. Soc.*, 51(3), 625–651.

Meng, L., J.-P. Ampuero, M. T. Page, and K. W. Hudnut (2011a), Seismological evidence and dynamic model of reverse rupture propagation during the 2010 M7.2 El Mayor Cucapah earthquake, Abstract S52B-04 presented at 2011 Fall Meeting, AGU, San Francisco, CA, USA, 5–9 Dec.

Meng, L., A. Inbal, and J.-P. Ampuero (2011b), A window into the complexity of the dynamic rupture of the 2011 Mw 9 Tohoku-Oki earthquake, *Geophys. Res. Lett.*, 38, L00G07, doi:10.1029/2011GL048118.

Nakahara, H. (2008), Seismogram envelope inversion for high-frequency seismic energy radiation from moderate-to-large earthquakes, in *Advances in Geophysics*, vol. 50, edited by R. Dmowska, pp. 401–426, Elsevier , Oxford, UK.

Nakahara, H., T. Nishimura, H. Sato, and M. Ohtake (1998), Seismogram envelope inversion for the spatial distribution of high-frequency energy radiation from the earthquake fault; application to the 1994 far east off Sanriku earthquake, Japan, *J. Geophys. Res.*, 103(B1), 855–867.

Nakahara, H., H. Sato, M. Ohtake, and T. Nishimura (1999), Spatial distribution of high-frequency energy radiation on the fault of the 1995 Hyogo-Ken Nanbu, Japan, earthquake (M_w 6.9) on the basis of the seismogram envelope inversion, *Bull. Seismol. Soc. Am.*, 89(1), 22–35.

Nakahara, H., T. Nishimura, H. Sato, M. Ohtake, S. Kinoshita, and H. Hamaguchi (2002), Broadband source process of the 1998 Iwate prefecture, Japan, earthquake as revealed from inversion analyses of seismic waveforms and envelopes, *Bull. Seismol. Soc. Am.*, 92(5), 1708–1720.

Okada, Y., K. Kasahara, S. Hori, K. Obara, S. Sekiguchi, H. Fujiwara, and A. Yamamoto (2004), Recent progress of seismic observation networks in Japan – Hi-net, F-net, K-NET and KiK-net, *Earth Planets Space*, 56(8), xv-xxviii.

Okamoto, J. (2012), Analysis of crustal deformation due to the 2010 Baja California earthquake, Mexico using SAR data, M.S. thesis, Dep. of Geophys., Kyoto Univ., Kyoto, Japan.

Oskin, M. E. et al. (2012), Near-field deformation from the El Mayor-Cucapah earthquake revealed by differential LIDAR, *Science*, 335(6069), 702–705, doi:10.1126/science.1213778.

Pollitz, F. F. (2003), Transient rheology of the uppermost mantle beneath the Mojave Desert, California, *Earth Planet. Sci. Lett.*, 215(1–2), 89–104, doi:10.1016/S0012-821X(03)00432-1.

Roten, D., H. Miyake, and K. Koketsu (2012), A Rayleigh wave back-projection method applied to the 2011 Tohoku earthquake, *Geophys. Res. Lett.*, 39(2), L02302, doi:10.1029/2011GL050183.

Rymer, M. J., et al. (2010), Triggered surface slips in Southern California associated with the 2010 El Mayor-Cucapah, Baja California, Mexico, earthquake, U. S. Geol. Survey Open File Report 2010–1333 and Calif. Geol. Survey Special Report 221.

Sato, T. (1994), Seismic radiation from circular cracks growing at variable rupture velocity, *Bull. Seismol. Soc. Am.*, 84(4), 1199–1215.

Savage, J. C. (1965), The stopping phase on seismograms, *Bull. Seismol. Soc. Am.*, 55(1), 47–58.

Savage, J. C., and H. S. Hasegawa (1964), Some properties of tensile fractures inferred from elastic wave radiation, *J. Geophys. Res.*, 69(10), 2091–2100.

Simons, M. et al. (2011), The 2011 magnitude 9.0 Tohoku-oki earthquake: Mosaicking the megathrust from seconds to centuries, *Science*, 332(6036), 1421–1425, doi:10.1126/science.1206731.

Spudich, P., and L. N. Frazer (1984), Use of ray theory to calculate high-frequency radiation from earthquake sources having spatially variable rupture velocity and stress drop, *Bull. Seismol. Soc. Am.*, 74(6), 2061–2082.

Suzuki, W., and T. Iwata (2009), Broadband seismic wave radiation process of the 2000 western Tottori, Japan, earthquake revealed from wavelet domain inversion, *J. Geophys. Res.*, 114(B8), B08302, doi:10.1029/2008JB006130.

Takeo, M. (1985), Near-field synthetic seismograms taking into account the effects of anelasticity – the effects of anelastic attenuation on seismograms caused by a sedimentary layer, *Pap. Meteor. Geophys.*, 36(4), 245–257.

Uchide, T., and S. Ide (2007), Development of multiscale slip inversion method and its application to the 2004 Mid-Niigata Prefecture earthquake, *J. Geophys. Res.*, 112(B6), B06313, doi:10.1029/2006JB004528.

Walker, K. T., and P. M. Shearer (2009), Illuminating the near-sonic rupture velocities of the intracontinental Kokoxili Mw 7.8 and Denali fault Mw 7.9 strike-slip earthquakes with global P wave back projection imaging, *J. Geophys. Res.*, 114(B2), B02304, doi:10.1029/2008JB005738.

Walker, K. T., M. Ishii, and P. M. Shearer (2005), Rupture details of the 28 March 2005 Sumatra Mw 8.6 earthquake imaged with teleseismic P waves, *Geophys. Res. Lett.*, 32(24), L24303, doi:10.1029/2005GL024395.

Wang, D., and J. Mori (2011), Frequency-dependent energy radiation and fault coupling for the 2010 Mw8.8 Maule, Chile, and 2011 Mw9.0 Tohoku, Japan, earthquakes, *Geophys. Res. Lett.*, 38(22), L22308, doi:10.1029/2011GL049652.

Wei, S. et al. (2011), Superficial simplicity of the 2010 El Mayor-Cucapah earthquake of Baja California in Mexico, *Nature Geosci*, *4*(9), 615–618, doi:10.1038/ngeo1213.

Wessel, P., and W. H. F. Smith (1991), Free software helps map and display data, *Eos Trans. AGU*, *72*(41), 441.

Yabuki, T., and M. Matsu'ura (1992), Geodetic data inversion using a Bayesian information criterion for spatial distribution of fault slip, *Geophys. J. Int.*, *109*(2), 363–375.

Yamashita, T. (1983), High-frequency acceleration radiated by unsteadily propagating cracks and its near-source geometrical attenuation, *J. Phys. Earth*, *31*(1), 1–32.

Yao, H., P. Gerstoft, P. M. Shearer, and C. Mecklenbräuker (2011), Compressive sensing of the Tohoku-oki M_w 9.0 earthquake: Frequency-dependent rupture modes, *Geophys. Res. Lett.*, *38*(20), L20310, doi:10.1029/2011GL049223.

Yao, H., P. M. Shearer, and P. Gerstoft (2012), Subevent location and rupture imaging using iterative backprojection for the 2011 Tohoku M_w 9.0 earthquake, *Geophys. J. Int.*, *190*, 1152–1168, doi:10.1111/j.1365-246X.2012.05541.X.

Zeng, Y. H., K. Aki, and T. L. Teng (1993), Mapping of the high-frequency source radiation for the Loma-Prieta earthquake, California, *J. Geophys. Res.*, *98*(B7), 11981–11993.

Zheng, Y., J. Li, Z. Xie, and M. H. Ritzwoller (2012), 5Hz GPS seismology of the El Mayor–Cucapah earthquake: Estimating the earthquake focal mechanism, *Geophys. J. Int.*, *190*(3), 1723–1732, doi:10.1111/j.1365-246X.2012.05576.X.